29th Congress of the International Council of the Aeronautical Sciences
St. Petersburg, Russia; September 7-12, 2014

INVESTIGATION OF AIRFOIL FOR AN INSECT-SIZED FLAPPING WING

Hiroto Nagai*, Koji Isogai*, Nobuhide Uda*, Kosei Ono*
***Kyushu University**

Keywords: *Flapping Wing, Insect Airfoil, Morphing Airfoil, CFD, Corrugation*

Abstract

We have conducted numerical study for a 3D flapping wing in hovering using computational fluid dynamics, considering airfoils of a bumblebee and a morphing airfoil by controlling a hinge angle connecting the fore- and hindwings. The aerodynamic effects of insect airfoils have been investigated in addition to the effect of the variable-cambered flapping airfoil. The corrugation of a bumblebee is little effective on aerodynamic characteristics of a flapping wing. Positive cambered airfoils are effective on the aerodynamic characteristics. However, the effect is canceled out in the up- and downstrokes. As a result, the airfoils of the bumblebee do not exceed the flat plate airfoil in time-averaged aerodynamic characteristics for a flapping cycle, if the airfoil is rigid. By controlling the hinge angle connecting the fore- and hindwings, preferable camber can be attained in both the up- and downstrokes. As a result, the hinge-controlled variable-camber airfoil shows about 14% increase in the time-averaged lift coefficient compared to the rigid flat airfoil.

1 Introduction

Insects are flying in viscous fluid at a low Reynolds number less than 10^4 because of their small sizes. Nevertheless, they have outstanding flight maneuverability and stability even in open air. So far, many studies have clarified the unsteady aerodynamic phenomena in insect flapping flight, such as *delayed stall*, *rotational circulation*, *wake capture*, and *clap-and-fling* [1–3]. Those aerodynamic mechanisms enhance lift in such a low Reynolds number regime by utilizing vortices around the wings. The outstanding flight ability of insects has attracted many researchers for the purpose of developing an insect-sized Micro Air Vehicle (MAV). Although some flapping type MAVs have succeeded in free flight [4], they have not yet attained comparable flight performance to that of insects. There may be any other novel techniques in insect flight we have not yet known.

A flapping wing, unlike a fixed wing, is subjected to inflows from the upper surface in the upstroke and the lower surface in the downstroke. In addition, a flapping wing experiences large flow separation from the leading-edge and reattachment because it is usually used at a high angle of attack near 45 deg. For these reasons, a cambered, corrugated, asymmetric airfoil, has been considered to be little effective on the aerodynamic characteristics for an insect-sized flapping wing. In fact, many studies for flapping wings have been conducted by using symmetrical flat plate models [1–3, 13–15].

As is well known, insects have complicated airfoil shapes. The corrugated airfoils of dragonflies contribute to improving the aerodynamic characteristics in gliding flight [5–7]. Although bumblebees cannot fly stopping their wings, they have large cambered and corrugated airfoils. Obviously, a cambered or corrugated airfoil enhances the rigidity of the wing structure; therefore, it contributes to the lightweight wing [8]. Aerodynamic effects of airfoils for an insect-sized flapping wing have not been investigated enough. Dickinson et al. have measured fluid force acting on a two-dimensional wing with a camber when the wing was translated at fixed angles of attack at a

Reynolds number of 197 [9]. Usherwood and Ellington have measured aerodynamic force acting on two kinds of cambered wing in propeller-like rotation at fixed angles of attack at a Reynolds number of 8071 [10]. Luo and Sun have calculated unsteady aerodynamic force using computational fluid dynamics for three-dimensional flapping wing with a simple corrugated airfoil modeled by triangular waves at Reynolds numbers of 200 and 3500 [11]. These studies have reported that the cambered or corrugated airfoils were little effective on aerodynamic force for a flapping wing compared to a flat plate. However, their wing models were very simple and not modeled on the realistic airfoils of insects.

A bumblebee has two pairs of fore- and hindwings shown in Fig. 1. There are many small hooks standing in a row at the leading-edge of the hindwing as shown in Fig. 2. The hooks are connected to the trailing-edge of the forewing when the wings are spread. Therefore, the hindwing cannot be moved independently of the forewing. However, the hooks play a role as a hinge; the hinge angle between the fore- to hindwings can be changed. We have observed the wing motion of a bumblebee by using a high-speed video camera and confirmed that some variation of the hinge angle occurred during a flapping cycle, though any quantitative data has not been acquired. Controlling the hinge angle between the fore- and hindwings causes the airfoil shape to be varied during a flapping cycle, that is, a morphing flapping airfoil. So far, any studies for a flapping wing considering a hinge connecting the fore- and hindwings have not conducted as far as we know.

In this study, we conduct a numerical study using computational fluid dynamics for a 3D insect-sized flapping wing with realistic airfoils of a bumblebee. First, the aerodynamic effect of the bumblebee's airfoils are investigated when the airfoil is considered to be rigid. Second, we conduct numerical simulation for a 3D flapping wing with a morphing airfoil, which is achieved by actively controlling a hinge angle connecting fore- and hindwings. The aerodynamic effect of the hinge-controlled airfoil are investigated.

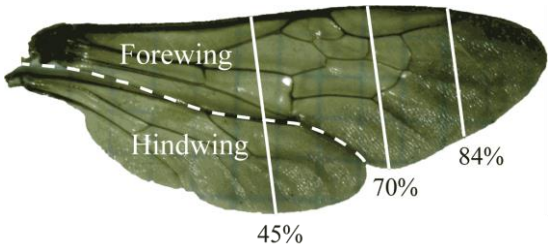

Fig. 1. Planform of bumblebee wings.

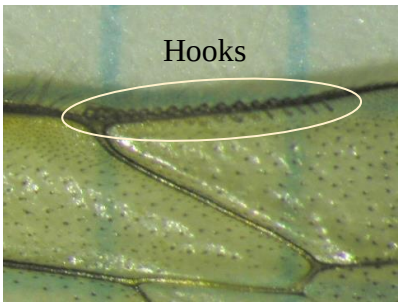

Fig. 2. Hooks at the leading-edge of the hindwing of a bumblebee.

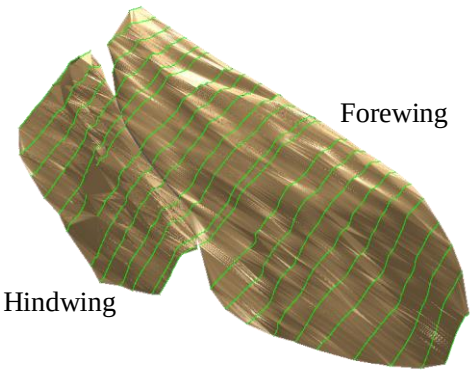

Fig. 3. 3D wing shape for a bumblebee.

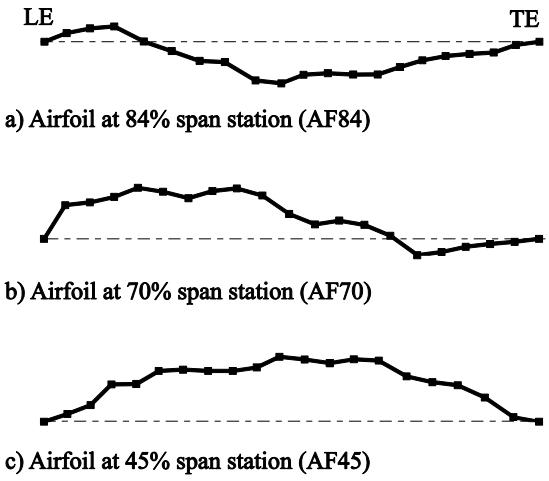

Fig. 4. Representative airfoils at three span stations for a bumblebee wing.

2 Materials and Methods

2.1 Measurement of Insect Airfoil

Bumblebees show an outstanding flight performance compared to any other insects, such as hovering, fast flight, and quick turning. In this study, the airfoils of a bumblebee, *bombus terrestris*, were employed to investigate the aerodynamic effect. The planform of a bumblebee's wing are shown in Fig. 1. In this study, we consider a pair of the fore- and hindwings as a single wing because the hindwing cannot be moved independently of the forewing. We confirmed that the planform shape and venation pattern of bumblebees are similar among individuals, though the span length varies from about 10 to 16 mm. Measurement of the three-dimensional shape of the bumblebee wing is conducted by using a laser probe 3D measuring instrument with 1 nm scale resolution (NH – 3SP, Mitaka Kohki. Co., Ltd., Japan). Since the wing is very thin, vacuum gold evacuation coating was done on a wing surface to help laser reflecting. The measurement was done in each 2 μm step in chordwise direction at 23 span stations. The three-dimensional surface of the wing was made based on the measured data using 3D CAD software (CATIA), shown in Fig. 3. The airfoils near the wing base have large camber and corrugation. Figure 4 shows three representative airfoils at 84%, 70%, and 45% semi-span station (hereinafter called AF84, AF70, and AF45, respectively). The data shown in Fig. 4 are reduced to 21 points by smoothing process. The three representative airfoils have different shapes: a large positive camber (12.7%) at AF45, a reflexed camber at AF70, and a small negative camber (-5.5%) at AF84.

2.2 Flapping Wing Kinematics

The coordinate of a 3D flapping wing is defined as shown in Fig. 5. The wing kinematics of insects mainly consists of a flapping motion (up- and downstrokes) and a feathering motion (supination and pronation). Based on the wing kinematics of bumblebees [12], the time histories of flapping and feathering angular

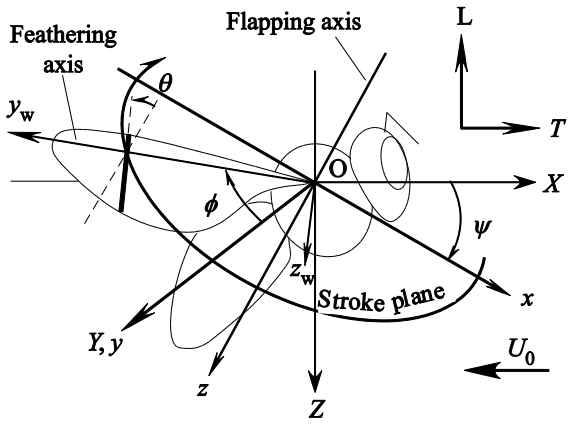

Fig. 5. Coordinate systems for a 3D flapping wing.

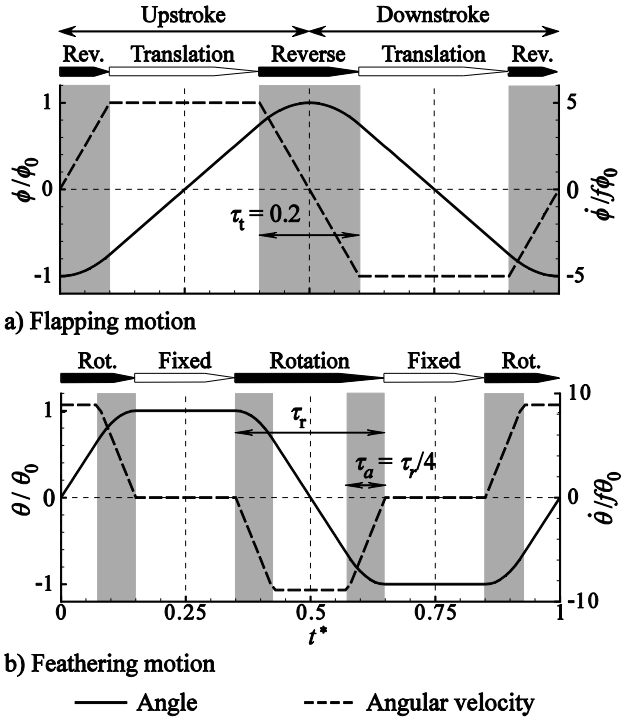

Fig. 6. Time histories of wing kinematics for a flapping cycle

velocities are represented as trapezoidal functions shown in Figs. 6a and 6b, respectively. Here, the non-dimensional time t^* is normalized by a flapping cycle. The flapping motion consists of translational and reversal phases. In the translational phase, the wing is moved at a constant angular velocity. In the reversal phase, the wing is decelerated and accelerated around the stroke reversal (t^* = 0.0, 0.5, and 1.0). The duration of the reversal phase is denoted by a non-dimensional time τ_t. The feathering motion consists of fixed-angle and rotational phases. In the fixed-angle phase, the wing moves at a

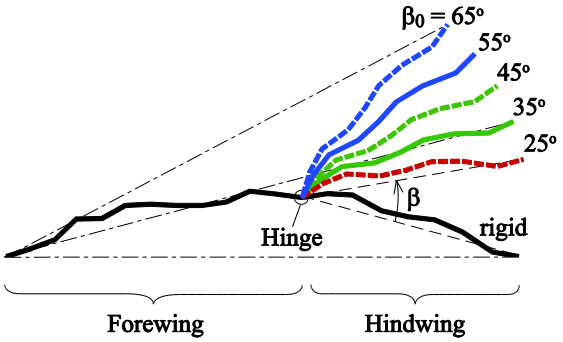

Fig. 7. The airfoil AF45 with hinge control.

constant angle of attack. In the rotational phase, the wing rotates around the span axis of the wing. The duration of the rotational phase is denoted by a non-dimensional time τ_r. In this study, τ_t = 0.2, τ_r = 0.2 based on the wing kinematics of bumblebees [12]. The amplitude of flapping angle ϕ_0 is 60 deg; the amplitude of feathering angle θ_0 is varied from 5 to 80 deg with 5 deg increments. The feathering rotation was conducted symmetrically with respect to the stroke reversal, called *symmetrical rotation*.

2.3 Hinge-Controlled Airfoil Model

A morphing airfoil was considered by controlling a hinge angle connecting fore- and hindwings during a flapping cycle. The hinge angle β is defined as a rotating angle abound the hinge axis from the position of the original rigid airfoil. A positive β means a rotation to the upper surface side. The hinge angle β was actively controlled until the amplitude of hinge angle β_0 was reached. The time history of β/β_0 is the same as that of the feathering motion shown in Fig. 6b. The timing of hinge rotation with respect to the feathering motion is denoted by a non-dimensional time difference τ_{fh}. When the hinge rotation is made at the same timing as the feathering rotation, it is called symmetrical hinge rotation and τ_{fh} = 0. When it starts earlier than the feathering rotation, it is called advanced hinge rotation (τ_{fh} < 0); when it starts later than the feathering rotation, it is called delayed hinge rotation (τ_{fh} > 0). In this paper, the hinge control was applied to the airfoil AF45 and a flat plate. Actually, the airfoil at 45% span station consists of fore- and hingwings with a hinge connection as shown in

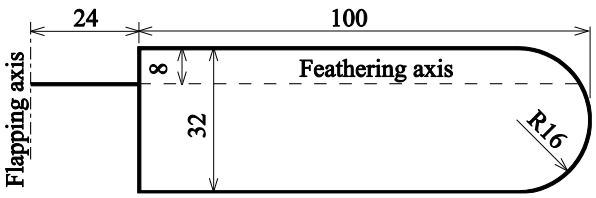

Fig. 8. Planform for numerical simulation.

Fig. 1. If the airfoil AF45 is rigid with no hinge, it has a positive camber in the downstroke but a negative one in the upstroke. However, if we control the hinge angle in the upstroke, a positive cambered airfoil can be attained in the upstroke. Figure 7 shows some examples for the airfoil AF45 when the hindwing is rotated to the upper side. When the hinge angle is greater than 35 deg, the airfoil has an opposite camber, that is, a positive camber in the upstroke. In this study, the hinge of the airfoil AF45 was controlled only in the upstroke and not controlled in the downstroke. The hinge angle of flat plate was controlled with the same amplitude of hinge angle β_0 in both the up- and downstrokes.

2.4 Numerical Method

Numerical simulation for a 3D flapping wing with an insect airfoil was conducted using an originally developed 3D Navier-Stokes code [13]. The 3D NS code has been validated for 3D flapping wings with a flat airfoil in hovering and forward flight in Ref. [13–15]. A Body fitted H–H type grid were used around an airfoil. The far-field boundaries were located at a distance of 15 chord lengths in the *Z*-direction and 5 span lengths in the *Y*-direction. At the *X*-*Z* plane, a symmetry condition was applied. The number of grid points was 160 points in the chordwise direction (60 points on the airfoil), 35 points in the span-wise direction (25 points on the wing) and 62 points normal to the wing surface. A no-turbulence model was used because of a low Reynolds number regime.

For simplicity, the test wing had a rectangular planform with a circular wing tip as shown in Fig. 8. Note that the size of the test wing was based on a scale model for experiment conducted in future work. The aspect ratio of the test wing was 6.25 based on that of the

bumblebee of 6.55. A test wing employs the same airfoil shape at any span station, which was one of the three airfoils of the bumblebee or a flat plate. The test wing was rigid with no elastic deformation.

A computation was conducted for four flapping cycles in hovering flight at the stroke plane angle $\psi = 0$. Lift L and drag D are defined as vertical and horizontal aerodynamic forces, respectively. The aerodynamic torques around the flapping axis, feathering axis, and hinge axis are denoted by Q_ϕ, Q_θ, and Q_β, respectively. The aerodynamic power is given by,

$$P_\phi = Q_\phi \dot{\phi}, \quad P_\theta = Q_\theta \dot{\theta}, \quad P_\beta = Q_\beta \dot{\beta} \qquad (1)$$

In this study, negative aerodynamic power was neglected because we consider that it cannot be stored. Time-averaged aerodynamic power is an integration of the positive aerodynamic power of Eq. 1 during a flapping cycle, given by,

$$\overline{P} = \int_0^1 \left(P_\phi^+ + P_\theta^+ + P_\beta^+\right) dt^* \qquad (2)$$

The time-averaged $\overline{L}$, $\overline{D}$, and $\overline{P}$ for a flapping cycle were non-dimensionalized by using a fluid density, a wing area, and a reference velocity V_0; then, time averaged coefficients of $\overline{C}_L$, $\overline{C}_D$, and $\overline{C}_P$ are obtained. The reference velocity V_0 is defined based on the flapping velocity at 2/3 semi-span location as follows,

$$V_0 = 2\pi f \phi_0 r \qquad (3)$$

where, f is the flapping frequency of 0.25 Hz, and r is the distance from the flapping axis to the 2/3 semi-span station of 90.7 mm. The Reynolds number based on the reference velocity V_0 and the semi-chord length was 2387, which is close to the Reynolds number of a bumblebee of 1980 [12].

3 Results and Discussion

3.1 Aerodynamic Characteristics of Rigid Insect Airfoils

In this section, we conducted numerical simulation for the three rigid airfoils of the bumblebee shown in Fig. 4. Figure 9 shows the time histories of C_L during a flapping cycle for the three airfoils of the bumblebee when $\theta_0 = 45$ deg. For comparison, C_L for a flat plate is added in Fig. 9. The waveform of C_L for the flat plate is quite the same in the up- and downstrokes. C_L for AF84 is larger in the upstroke and smaller in the downstroke than that for the flat plate. On the other hand, C_L for AF45 and AF70 are larger in the upstroke and smaller in the downstroke than that for the flat plate. The non-dimensional vorticity around the three airfoils and flat plate (at 50% span station of the rectangular test wing) at the center of each stroke (t^* = 0.25 and 0.75) are shown in Figs. 10a–10f, and 10j. For all of the airfoils, there is a large leading-edge vortex (LEV) attached on the upper surface, which result in large lift generation in the low Reynolds number regime. However, there are differences in the strength of LEV and the surface direction subjected to the LEV. The LEV is stronger for the positive cambered airfoil whereas it is weaker for the negative cambered airfoil than that of the flat plate. The positive cambered airfoils are subjected to low pressure caused by the LEV on the surface directed upward; as a result, the suction force caused by the LEV contributes to lift. On the other hand, the negative cambered airfoils are subjected to the low pressure on the surface directed backward; as a result, the suction force contributes to drag. The airfoil AF70 has a large camber near the leading-edge but a reflected camber near the trailing-edge. Therefore, the LEV around AF70 in the downstroke is weaker than that for AF45, as shown in Figs. 10d and 10f.

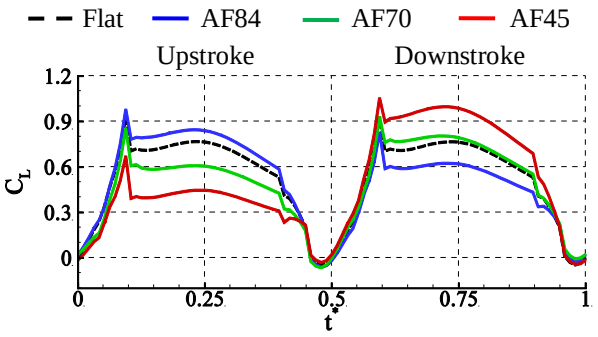

Fig. 9. Time histories of C_L for the three airfoils of the bumblebee.

The delayed stall effect due to a LEV contributes to a large part of the total lift produced by an insect-sized flapping wing [15].

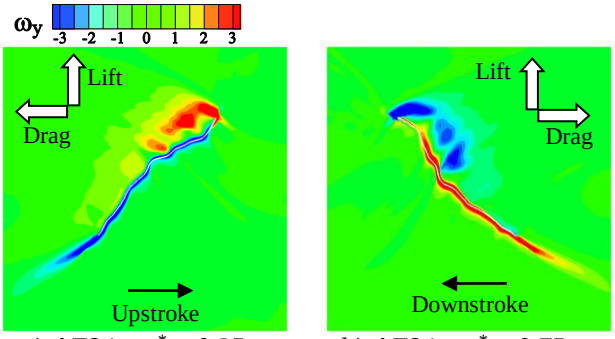

a) AF84 at t^* = 0.25 b) AF84 at t^* = 0.75

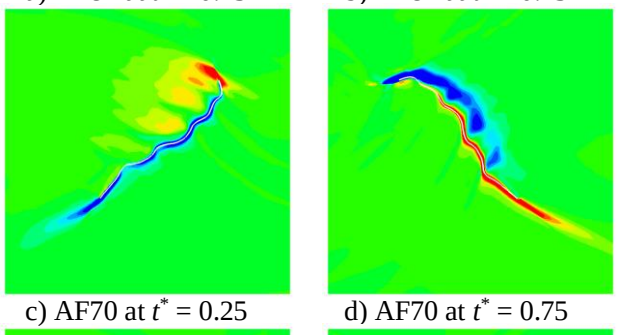

c) AF70 at t^* = 0.25 d) AF70 at t^* = 0.75

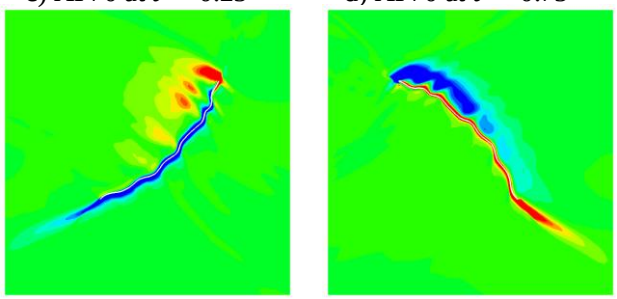

e) AF45 at t^* = 0.25 f) AF45 at t^* = 0.75

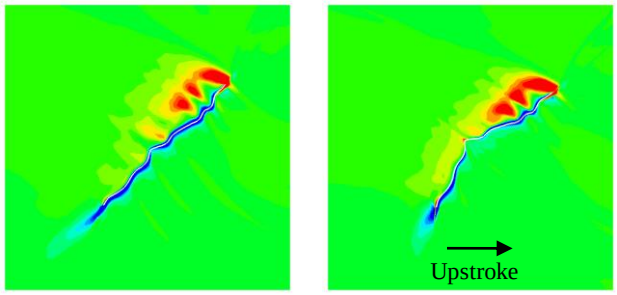

g) Hinge-controlled AF45 for β = 35° at t^* = 0.25 h) Hinge-controlled AF45 for β = 65° at t^* = 0.25

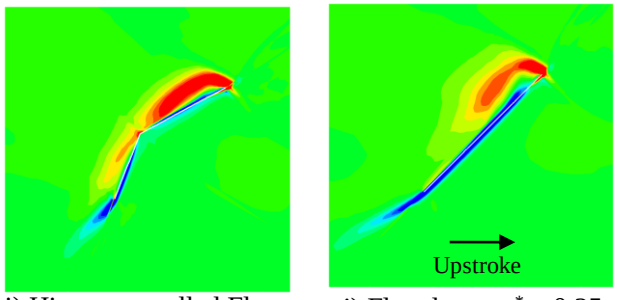

i) Hinge-controlled Flat plate for β = 40° at t^* = 0.25 j) Flat plate at t^* = 0.25

Fig. 10. Non-dimensional vorticity distribution around airfoils at 50% span station.

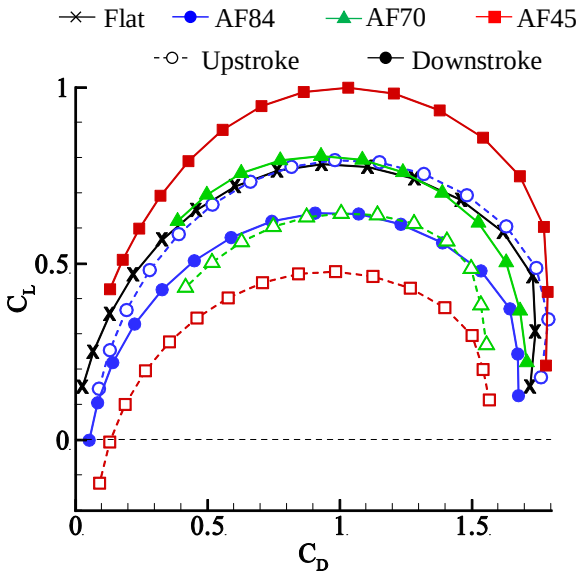

Fig. 11. Polar curve of C_L vs. C_D at the center of each stroke (t^* = 0.25 and 0.75) for the three airfoils of the bumblebee.

Around the center of each stroke, the delayed stall is dominant on lift generation whereas the other unsteady aerodynamic phenomenon is little effective. In order to evaluate the effect of airfoils on the forces due to the delayed stall, the aerodynamic characteristics at the center of each stroke are compared for the three airfoils of the bumblebee. Figure 11 shows the polar curve of C_L vs. C_D for the airfoils at the center of each stroke when the amplitude of feathering angle θ_0 is varied from 5 to 80 deg with 5 deg increments. Note that the angle of attack $\alpha = \pi/2 - \theta_0$ in hovering flight. As shown in Fig. 11, the polar curve is shifted to the upper side for the positive camber airfoils and lower side for the negative camber airfoils than that of the flat plate. The result indicates that the three airfoils of the bumblebee show a better aerodynamic characteristics in one stroke when the airfoil becomes a positive camber but a worse characteristics in the other stroke when the airfoil becomes a negative camber. From Fig. 11, it can be easily seen that the averaged curve between the up- and downstrokes for each bumblebee's airfoil is lower than that of the flat plate, even if any combination of the amplitudes of feathering angles between the up- and downstrokes is considered. The fact indicates that the camber effect on the aerodynamic force

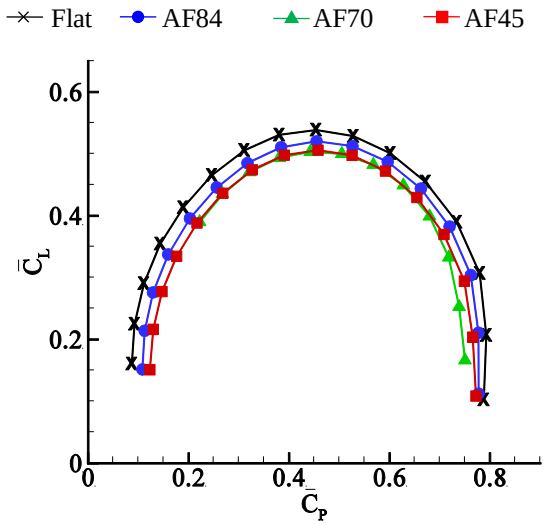

Fig. 12. Polar curve of time-averaged C_L vs. C_P for the airfoils of the bumblebee.

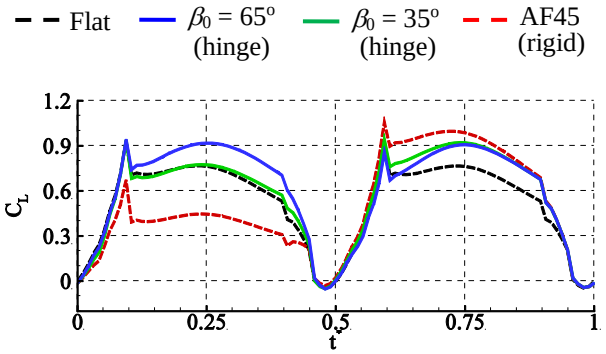

Fig. 13. Time histories of C_L for the hinge-controlled airfoils AF45.

due to the delayed stall is cancelled out between the up- and downstrokes.

Figure 12 shows the polar curve of time-averaged $\bar{C}_L$ vs. $\bar{C}_P$ for a flapping cycle when the amplitude of fathering angle is the same in both the up- and downstrokes. Figure 12 also indicates that the three airfoils of the bumblebee does not exceed the flat plate airfoil in the time-averaged aerodynamic characteristics, even though the other unsteady aerodynamic effects are included in addition to the delayed stall.

3.3 Aerodynamic Characteristics of Hinge-controlled Airfoils

In this section, we conducted numerical simulation for the variable-cambered airfoils by controlling the hinge angle. Figure 13 shows the time histories of C_L during a flapping cycle for the airfoil AF45 with hinge control. Note that

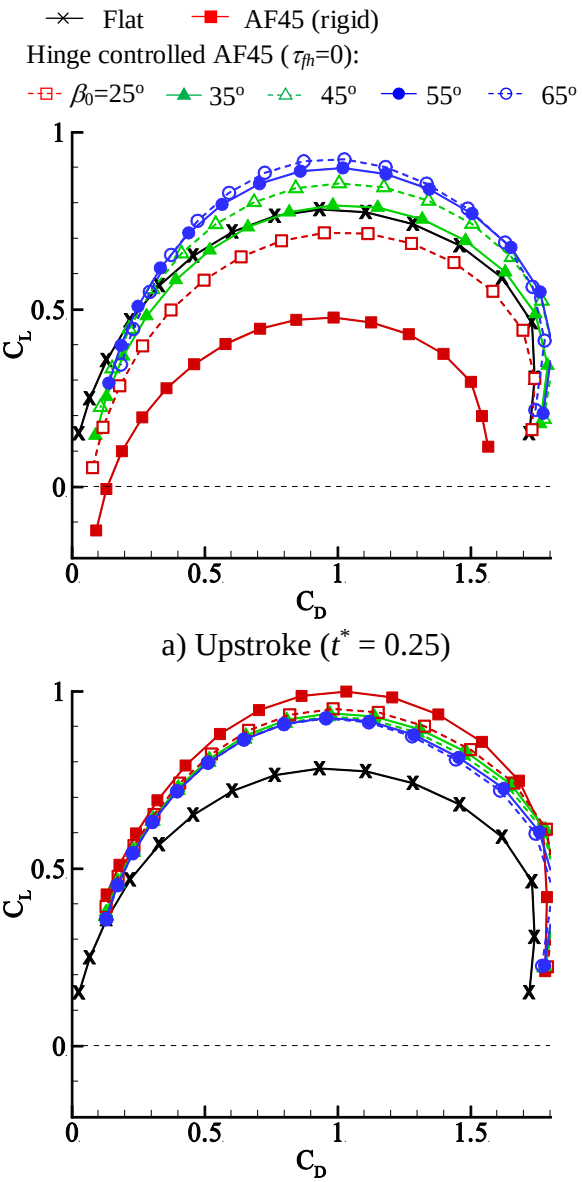

a) Upstroke (t^* = 0.25)

b) Downstroke (t^* = 0.75)

Fig. 14. Polar curve of C_L vs. C_D at the center of each stroke with respect to hinge angle β_0 for hinge-controlled airfoils AF45.

the hinge is controlled only in the upstroke and not controlled in the downstroke. The hinge-controlled airfoil AF45 generates larger lift than the flat plate in both the up- and downstroke. Although the airfoil shapes for the hinge-controlled airfoils are quite the same as the rigid airfoil in the downstroke, C_L for the hinge-controlled airfoil is slightly smaller than that for the original AF45 in the downstroke. This phenomenon is attributed to enhancement of the downwash caused by increasing lift in the upstroke. Despite of decreasing lift in the

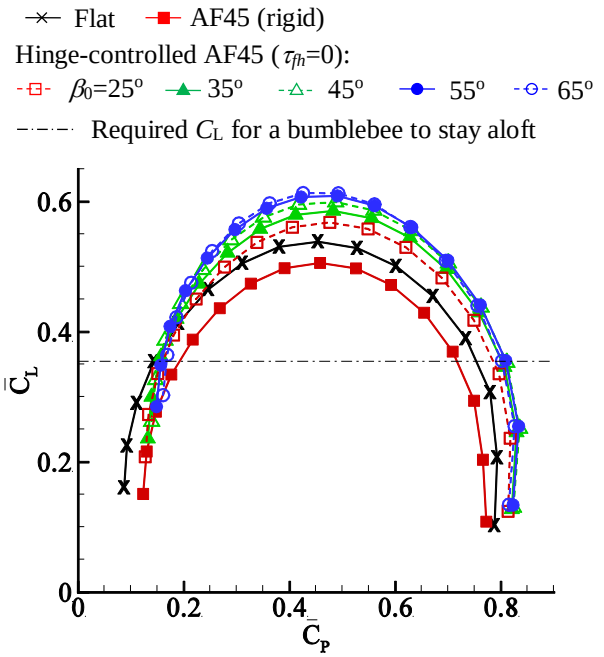

Fig. 15. Polar curve of time-averaged C_L vs. C_P with respect to hinge angle for hinge-controlled AF45.

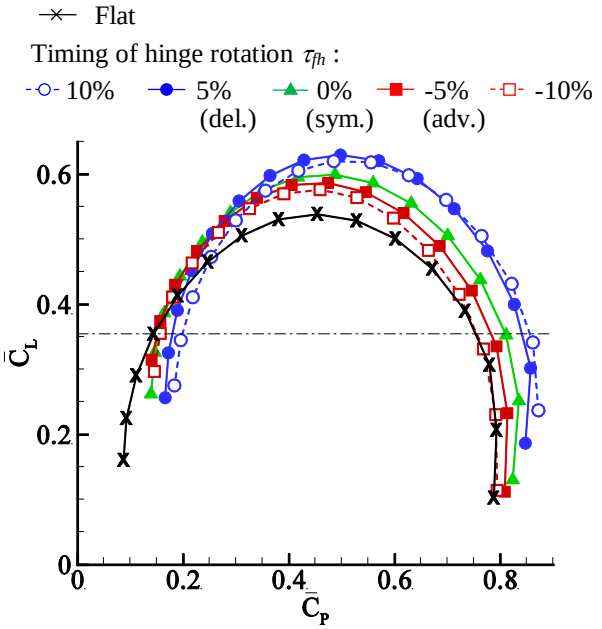

Fig. 16. Polar curve of time-averaged C_L vs. C_P with respect to timing of hinge rotation τ_{fh} for hinge controlled AF45 with β_0 =45°.

downstroke, the time-averaged lift for the hinge-controlled airfoil is larger than that for the flat plate. Figures 10g and 10h show the vorticity in the upstroke for the hinge-controlled AF45 with β_0 = 35 and 65 deg. Compared to the flow for the rigid airfoil AF45 shown in Fig. 10e, the hinge-controlled airfoil enhances the strength of the leading-edge vortex in the upstroke.

Figure 14 shows the polar curve of C_L vs. C_D at the center of the up- and downstrokes for the hinge-controlled airfoil AF45. As the hinge angle increases, C_L in the upstroke increases but slightly decreases in the downstroke. The two curves for β_0 = 55 and 65 deg are almost the same, which means that the optimal β_0 is near that angles. As shown in Fig. 7, the hinge-controlled airfoil at β_0 = 35 deg has smallest camber, which is considered to be a corrugated airfoil with no camber. As shown in Fig. 14a, the AF45 for β_0 =35 deg shows almost the same polar curve as the flat plate in the upstroke. This fact indicates that the corrugation of the airfoil is not effective on the aerodynamic force, which agrees with the result by Luo and Sun [11].

Figure 15 shows the polar curve of time-averaged $\bar{C}_L$ vs. $\bar{C}_P$ for a flapping cycle for the hinge-controlled airfoil AF45. The horizontal dotted line means the required $\bar{C}_L$ (= 0.355) for a bumblebee to stay aloft, which was calculated based on the measured data for the bumblebee *BB01* described in Ref. [12]. In the range at the larger amplitude of the feathering angle, or the smaller angle of attack, the polar curve for the flat plate is upper than the hinge-controlled airfoils; however, $\bar{C}_L$ is not reached to the required $\bar{C}_L$ for a bumblebee in that range. In the range beyond the required $\bar{C}_L$ for a bumblebee, the hinge-controlled airfoil shows higher aerodynamic characteristics than the flat plate. The maximum $\bar{C}_L$ for the hinge-controlled AF45 with β_0 = 65 deg is 13.8% larger than that of the flat plate and 21.3% larger than that of the original rigid AF45.

As described previous works [2, 15], the timing of feathering rotation with respect to the flapping reversal is significantly effective on the aerodynamic characteristics. Here, we have investigated the effect of the timing of hinge rotation on the aerodynamic characteristics. Figure 16 shows the polar curve of time-averaged $\bar{C}_L$ vs. $\bar{C}_P$ for the hinge-controlled airfoil AF45 with β_0 = 45 deg when the timing of hinge rotation τ_{fh} is varied. In the advanced

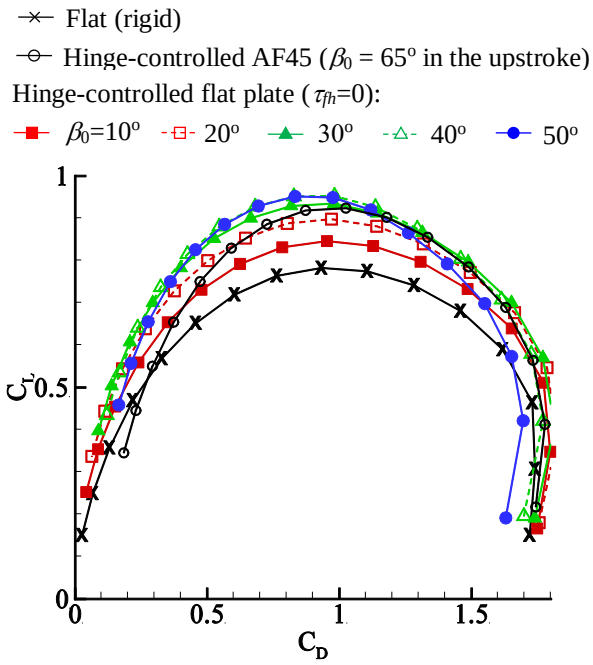

Fig. 17. Polar curve of C_L vs. C_D with respect to hinge angle for hinge-controlled flat plate.

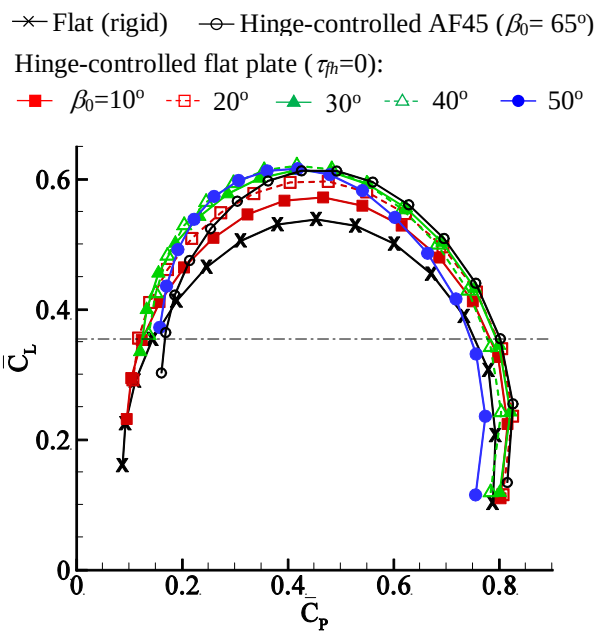

Fig. 18. Polar curve of time-averaged C_L vs. C_P with respect to hinge angle for hinge-controlled flat plate.

hinge rotation (τ_{fh} < 0), $\bar{C}_L$ is almost the same and $\bar{C}_P$ decreases slightly compared to those for the symmetrical hinge rotation (τ_{fh} = 0). In the delayed hinge rotation (τ_{fh} > 0), the maximum $\bar{C}_L$ increases though $\bar{C}_P$ also increases. The aerodynamic characteristics for each timing of the hinge rotation is better than that of the flat plate in the range beyond the required $\bar{C}_L$ for a bumblebee. Dislike the timing of feathering rotation, the aerodynamic characteristics is not sensitive to the timing of hinge rotation τ_{fh}. These facts are useful for a MAV to realize such a variable-cambered flapping airfoil by controlling the hinge angle.

Next, we conducted numerical simulation for a hinge-controlled flat plate airfoil. The hinge axis is located on 58% chord length from the leading-edge, which is the same as that of AF45 of the bumblebee. In this case, the hinge angle was controlled symmetrically in both the up- and downstrokes. The polar curves of C_L vs. C_D at the center of the stroke for the hinge-controlled flat airfoils are shown in Fig. 17 in addition to the best curve for the hinge-controlled AF45 with β_0 = 65 deg, which shows the maximum C_L in Fig. 14a. The hinge-controlled flat airfoil shows better aerodynamic characteristics at the almost all of the angle of attack. As the hinge angle increases, the polar curve shifts upper direction. The polar curves for β_0 = 30, 40, and 50 deg are almost the same, which means the optimal β_0 is in that range. The hinge-controlled flat airfoil has almost the same curve as the hinge-controlled AF45 at larger angles of attack. However, the flat airfoil generates larger lift with smaller power at small angles of attack. This fact indicates that the corrugation of the airfoil causes increasing drag at small angles of attack.

The polar curves of time-averaged $\bar{C}_L$ vs. $\bar{C}_P$ for the hinge-controlled flat airfoils are shown in Fig. 18 in addition to the best curve for the hinge-controlled AF45 with β_0 = 65 deg. The polar curve for the hinge-controlled flat airfoils is higher than that of the flat rigid plate at almost all of the feathering angles. The maximum values of $\bar{C}_L$ and the corresponding $\bar{C}_P$ are almost the same between the hinge-controlled flat and AF45 airfoils. This result also indicates that the corrugation of the bumblebee's airfoil is little effective on the aerodynamic characteristics, though there is a small difference in $\bar{C}_P$ at small angles of attack.

The maximum $\overline{C_L}$ for the hinge-controlled flat plate with β_0 = 40 deg is 14.7% larger than that of the rigid flat plate. The corresponding flow pattern around the airfoil is shown in Fig. 10i.

4 Conclusions

We have conducted numerical study for a 3D flapping wing in hovering using computational fluid dynamics, considering the airfoils of a bumblebee and a morphing airfoil by controlling a hinge angle. The corrugation of a bumblebee is little effective on aerodynamic characteristics of a flapping wing, though it causes a slight increase of drag at small angles of attack. Positive cambered airfoils are effective on the aerodynamic characteristics. However, the effect is canceled out in the up- and downstrokes. As a result, the airfoils of a bumblebee do not exceed the flat plate airfoil in time-averaged aerodynamic characteristics, if the airfoil is rigid. By controlling the hinge angle connecting the fore- and hindwings, preferable camber can be attained in both the up- and downstrokes. As a result, the hinge-controlled variable-camber airfoil improves the aerodynamic characteristics of a flapping wing compared to the flat airfoil.

Although a corrugation is not effective on the aerodynamic characteristics of a flapping wing, it can obviously improve the structural rigidity of the wing, which causes light-weight of the wing. In this study, any inertial force has not been considered. The effect of an inertial force of a flapping wing is significantly important because an insect-sized flapping wing must be oscillated at a high frequency. In our future work, we will evaluate the effects of flapping airfoils including not only aerodynamic aspects but also structural aspects.

Acknowledgement

This study was supported by Japan Society for the Promotion of Science (JSPS) KAKENHI Grant-in-Aid for Young Scientists (B).

References

[1] Ellington CP, Van den Berg C, Willmott AP, and Thomas ALR. Leading-edge vortices in insect flight. *Nature*, 384, pp 626-630, 1996.

[2] Dickinson MH, Lehmann F-O and Sane SP. Wing rotation and the aerodynamic basis of insect flight. *Science*, 284, pp 1954-1960, 1999.

[3] Weis-Fogh T. Quick estimates of flight fitness in hovering animals, including novel mechanisms for lift production. *J. Exp. Biol.*. 59, pp 169-230, 1973.

[4] Keennon M, Klingebiel K, Won H, Andriukov A. Development of the nano hummingbird: A tailless flapping wing micro air vehicle. *Proc. 50th AIAA Aero. Sci. Meeting, Nashville*, AIAA2012-0588, 2012.

[5] Okamoto M, Yasuda K and Azuma A. Aerodynamic characteristics of the wings and body of a dragonfly. *J. Exp. Biol.*, 199, pp 281-294, 1996.

[6] Vargas A, Mittal R, Dong H. A computational study of the aerodynamic performance of a dragonfly wing section in gliding flight. *Bioinsp.Biomim.*,3,13p,2008.

[7] Obata A and Shinohara S. Flow visualization study of the aerodynamics of modeled dragonfly wings. *AIAA J.*, 47, 12, pp 3043-3046, 2010.

[8] Combes SA. Materials, structure, and dynamics of insect wings as bioinspiration for MAVs. *Encyclopedia of Aerospace Engineering*, 2010.

[9] Dickinson MH and Götz KG. Unsteady aerodynamic performance of model wings at low Reynolds numbers. *J. Exp. Biol.*, 192, pp 179-206, 1994.

[10] Usherwood JR and Ellington CP. The aerodynamics of revolving wings I. Model hawkmoth wings. *J. Exp. Biol.*, 205, pp 1547-1564, 2002.

[11] Luo G and Sun M. The effect of corrugation and wing planform on the aerodynamic force production of sweeping model insect flapping wing. *Acta Mech Sinica*, 21 pp 531-541, 2005.

[12] Dudley R and Ellington CP. Mechanics of forward flight in bumblebees I. Kinematics and morphology. *J. Exp. Biol.*, 148, pp 19-52, 1990.

[13] Isogai K, *et al*. Unsteady three-dimensional viscous flow simulation of dragonfly hovering. *AIAA J.*, 42, 10, pp 2053-2058, 2004.

[14] Nagai H, *et al*. Experimental and numerical study of forward flight aerodynamics of insect flapping wing. *AIAA J.*, 47, 3, pp 730-742, 2009.

[15] Nagai H and Isogai K. Effects of flapping wing kinematics on hovering and forward flight aerodynamics. *AIAA J.*, 49, 8, pp 1750-1762, 2011.

Copyright Statement